Small Structures

www.small-structures.com

RESEARCH ARTICLE OPEN ACCESS

Patterns of Gold Nanoparticles on Cholesteric Surfaces

Ines Gharbi[1,2,3] | Amit R. Dhawan[4] | Randall D. Kamien[5] | Maxim O. Lavrentovich[6,7] | Emmanuelle Lacaze[1]

[1]Sorbonne Université, CNRS, Institut des Nanosciences de Paris (INSP), Paris, France | [2]LR99ES16 Soft Matter Physics and Electromagnetic Modelling Laboratory, Faculty of Sciences of Tunis, University of Tunis El Manar, Tunis, Tunisia | [3]LR11ES26 Laboratory of Computer Science for Industrial Systems, National Institute of Applied Sciences and Technology, North Urban Center, Carthage University, Tunis, Tunisia | [4]Department of Physics, University of Oxford, Oxford, UK | [5]Department of Physics and Astronomy, University of Pennsylvania, Philadelphia, Pennsylvania, USA | [6]Department of Earth, Environment and Physics, Worcester State University, Worcester, Massachusetts, USA | [7]Department of Physics & Astronomy, University of Tennessee, Knoxville, Tennessee, USA

Correspondence: Ines Gharbi (ines.gharbi@insat.ucar.tn) | Randall D. Kamien (kamien@physics.upenn.edu) | Emmanuelle Lacaze (emmanuelle.lacaze@insp.jussieu.fr)

Received: 7 December 2025 | **Revised:** 10 February 2026 | **Accepted:** 4 March 2026

ABSTRACT

Controlling nanoparticle assembly in soft matter is an important objective in materials science and technology. Cholesteric liquid crystals (CLCs) constitute an exceptional template for this purpose, guiding nanoparticles into complex, organized superstructures. However, achieving large-scale superstructures and understanding the interplay of the governing forces remain a challenge. Here, we demonstrate the precise localization of gold nanoparticle (AuNP) monolayers within the modulated texture of a polymer-stabilized CLC. Using optical, electron, and atomic force microscopy combined with Landau-de Gennes energy simulations, we show and explain how AuNPs self-assemble into large-scale arch textures that replicate the underlying CLC undulations. The organization is dictated by a balance between the mitigation of elastic distortions in the CLC and the anchoring conditions imposed by the AuNP monolayer. This balance positions the nanoparticles in valleys, slightly displaced from the most elastically distorted regions, just below the air interface. This specific localization appears to be associated with a less tilted easy axis at the CLC-AuNP interface compared to nematic films, resulting in reduced local hexagonal ordering within the AuNP monolayers. Our work provides design principles for controlling nanoparticle assemblies across multiple length scales, from macroscopic architectures to nanoscale order, by exploiting the coupling between liquid crystal elasticity and surface anchoring.

1 | Introduction

The remarkable beauty of liquid crystals (LCs) [1, 2] and their widespread applications [3–5] have made them intensely studied since their discovery in 1888 [6]. Progress in the development of functionalized liquid crystals (LCs) [7, 8] and their integration with nanoparticles (NPs) [9] has paved new avenues for scientific exploration and commercial applications. NPs can be embedded in LCs to improve LC properties, as they can be specifically oriented or assembled by the surrounding LC, which leads to new optical or electro-optical properties [9, 10]. The anisotropy of LCs allows the formation of oriented NP chains [11, 12], oriented NP ribbons [13–17], and NP monolayers [18], easily modified by temperature variations through the LC phase transitions [19, 20]. Optimized application of these multicomponent systems, however, requires stable composites devoid of uncontrolled aggregation.

The long-term stability of composite systems can be achieved by assembling NPs in oligomer LCs [21–24] and in polymer-stabilized liquid crystals (PSLCs) [18, 25]. Due to their enhanced strength and stability, PSLCs have indeed generated significant research interest [26–28]. Associating NPs with PSLCs [18, 25] makes their response significantly faster and uniform across the matrix, rendering these materials suitable for photonic technologies [29, 30].

Several strategies enable the controlled assembly of nanoparticles (NPs) in liquid crystals (LCs). One approach involves carefully controlling ligand grafting [31–33] on their surface. Another

---

method utilizes specific zones within the LC film, such as topological defects [17, 34–36] that act as templates to confine NPs and generate various geometries [10]. LC superstructures can also guide the organization of NPs; for instance, helical cholesteric modulations induce the formation of spiral-like ribbons [21–24]. Recently, nematic or smectic films have been used to form NP monolayers at LC-air interfaces, which adopt hexagonal order and are conserved after polymerization. Cholesteric liquid crystals (CLCs) are particularly promising for templating NPs, offering superior control over shape and geometry, whether in films [29, 30] or droplets [37], and leading to modulated superstructures [21–24, 37] that create NP assembly templated by the CLC texture.

Here, we study a cholesteric modulated superstructure to understand the interplay between anchoring and elastic interactions that influence NP assembly and can lead to specific, organized NP assembly. By studying PSLCs/gold NPs (AuNPs) composites using a combination of polarized light microscopy (PLM), scanning electron microscopy (SEM), and atomic force microscopy (AFM), we precisely determine the preferred localization of the induced AuNP monolayers that are shown to form large-scale arch textures on top of the modulated superstructure. Using Landau-de Gennes energy simulation of the CLC modulated texture, we demonstrate that the localization of the AuNP monolayers fulfills the optimal balance between anchoring on the NP monolayers and replacement of the most elastically distorted CLC zones. We show that this balance localizes the AuNP monolayers slightly away from the most elastically distorted regions just below the air interface. In addition, we reveal that the CLC anchoring geometry at the AuNP surface induces disorder at a small scale in the monolayer structure as compared to the AuNP monolayer formed at the surface of nematic films [18] without modulated distortions.

Our results illustrate that the need to balance both elastic distortion mitigation and anchoring conditions in an LC imposes both NP assembly localization and local structure.

2 | Results

2.1 | Polymer-Stabilized Cholesteric Liquid Crystal (PSCLC) Films

The arch structure, characteristic of the CLC (see Supplementary Information Figure S1), was preserved in our PSCLC samples, as shown in Figure 1a. We stabilized the CLC film by polymerization after introducing a monomer and a photo-initiator and subsequently irradiating it with ultraviolet light (see Section 4). The elastic interactions between the polymer network and the LC [38, 39] under ultraviolet irradiation create the PSCLC matrix whose polymer structure mimics the initial CLC texture [25, 26]. In case of planar, unidirectional anchoring on the substrate (versus homeotropic anchoring at the air interface), the cholesteric helical axis is perpendicular to the substrate until a layer of thickness $p/2$ at the air interface is reached, where p is the helical pitch [40, 41]. There, the helical axis rotates to become approximately parallel to the air interface. The reorientation of the pitch axis near the air interface is shown via simulation in Figure 1b. In the region of the CLC near the air interface, the orientation of the molecules alternates between planar and homeotropic, leading to the observation of alternating bright and dark stripes in PLM (Figure 1a). The precise orientation of the helical axis in the top layer is determined by the anchoring direction on the substrate, the geometry of the air interface, and the number of helical turns perpendicular to the substrate before the top layer of $p/2$ thickness is reached. The CLC pitch orientation at the air interface consequently depends on the film thickness. Therefore, film nonuniformities lead to the rotation of the alternating bright and dark stripes and to arch formation in PLM (Figure 1a) [38, 39]. As a result, arches are also associated with color variations in PLM images (Figure 1a).

Figure 1b shows simulated undulations of the CLC-air interface. Figure 1c,d show the AFM topography map and height profile of a typical PSCLC film. We find surface undulations consistent with previous AFM measurements of similar CLC top layers [42, 43]. We found that the polymerization of the sample was homogeneous, as AFM measurements could be performed anywhere on it. We measured an undulation period $\Lambda = 17.3 \pm 0.6$, averaged over 59 measurements (Figure 1c), and an undulation depth of 81.5 ± 15nm (104 measurements, Figure 1d). The undulation period is similar to the period of the stripes observed in PLM, confirming that these undulations on the surface are a consequence of the top layer of the PSCLC film.

PLM on CLC and PSCLC structures shows that, within an arch, the stripe orientation with respect to the polarizer affects its optical characteristics (color and contrast). The rotation of the sample between fixed polarizers transforms the director orientation with respect to the polarizers and therefore its polarization response. To note this, a PSCLC sample was placed between crossed polarizers, and the same sample region was observed at different angles of the sample with respect to the polarizers, as shown in Figure 1e. The 0° orientation corresponds to the rubbing direction parallel to the polarizer (protocol detailed in Supplementary Information Figure S2). Here, the outer dark stripe is overlaid with black dotted lines, and the overlaid blue dotted line runs through the center of the bright stripe. The boundaries of the dark stripe are depicted with overlaid white and yellow dotted lines. Noting the angle between the polarizer and the sample rubbing direction, we observe that the outer dark region remains dark, but the contrast with the bright region varies. In particular, the bright region develops a thin dark region in the middle between 20° and 70°. At 70°, the stripes appear similar to 20°, and at 90°, they appear more like 0°. In the following section, we will establish that the dark stripes are the peaks, and the bright stripes are the valleys of the top layer undulations.

2.2 | PSCLC-AuNPs

Polymer-stabilized cholesteric liquid crystal films with gold nanoparticles (PSCLC-AuNPs) were obtained by spin-coating a CLC-monomer film onto a substrate, drop-casting AuNPs in toluene above it, and polymerizing under UV light after solvent evaporation (see Section 4, Photopolymerizable monomer–CLC mixture). The solvent evaporation rate was kept constant to ensure homogeneous AuNP distribution across the film surface. A region of a PSCLC-AuNPs film was imaged with PLM (Figure 2a) and SEM (Figure 2b). The deposition of AuNPs did not significantly alter the cholesteric structure. PLM images show

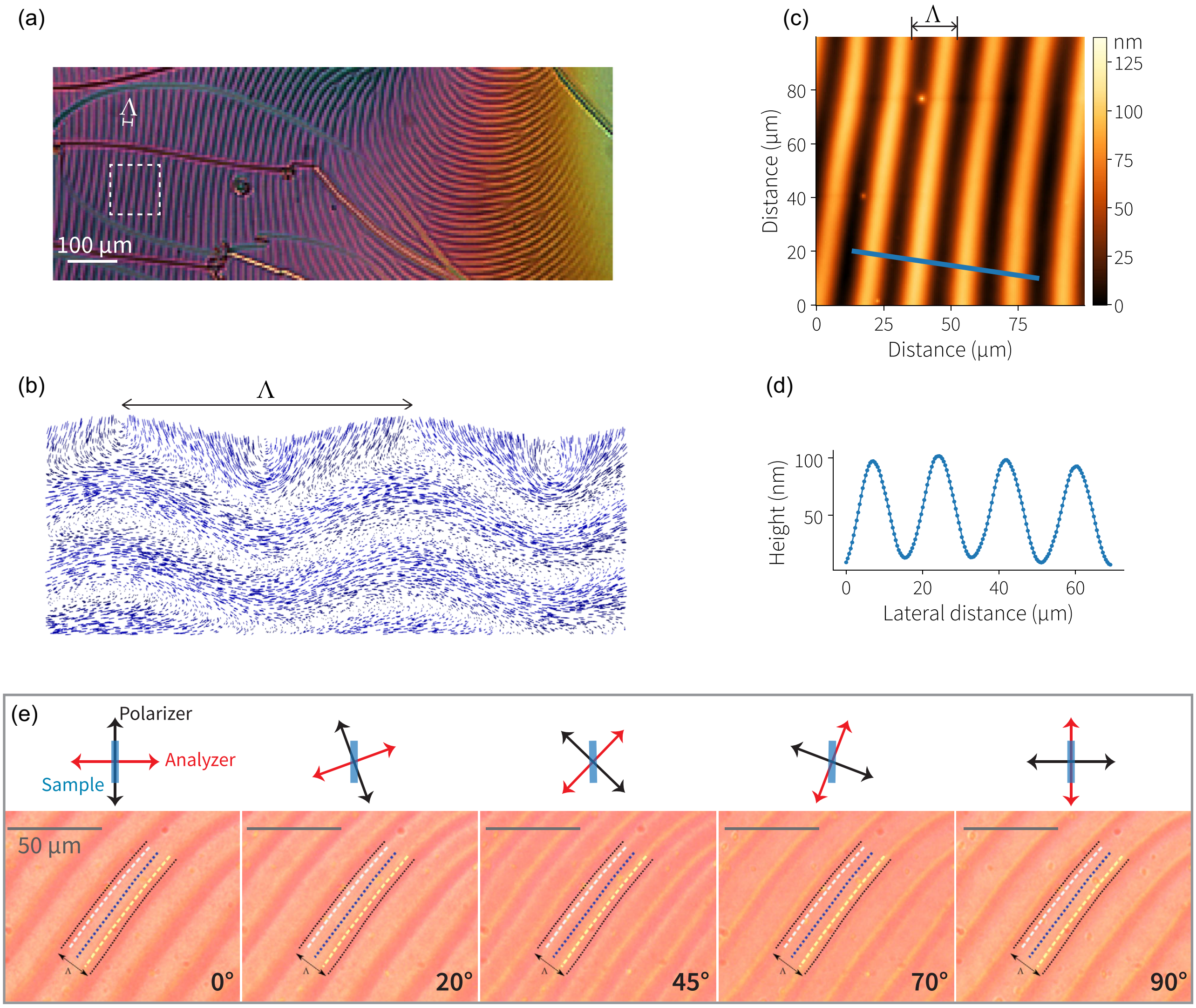

FIGURE 1 | (a) Crossed polarizer transmission light microscopy image of a CLC film with stripes of different colors that correspond to regions of different film thicknesses, and within each stripe, alternating dark and bright zones correspond to regions with different director orientations. Λ is the modulation period. (b) Simulated director fields in the top layer of a hybrid cholesteric film. (c) AFM image of the boxed region of the PSCLC film in (a), and its height profile (d) along the indicated direction. The undulation period Λ is shown in the images. (e) PSCLC film at different angles between crossed polarizers. The overlaid dotted lines highlight regions that can be compared between different polarizer orientations.

that the PSCLC-AuNPs film maintained both its modulation features and the stripes' evolution as a function of the light polarization angle (see Supplementary Information Figure S3). The AuNPs appear bright in SEM images due to the high mass of the Au atoms compared to the PSCLC molecules. They form periodic arches (Figure 2b) of the same period as the arches corresponding to alternating bright and dark arches as seen by PLM (Figure 2a). This demonstrates that the AuNPs were deposited in an organized manner along the arches formed by the PSCLC top layer. The white arches observed in Figure 2b are made of microscale islets (Figure 2c), which are themselves formed by monolayers of AuNPs, as shown in Figure 2d. The inset in Figure 2d shows the local organization of AuNPs in a monolayer. Our AuNP deposition method prevented the formation of aggregates in the arches, unlike previously reported with another method [22]. This demonstrates that it is possible to localize AuNPs favorably in a modulated superstructure by depositing them in a secondary step (see Section 4).

To understand the localization of AuNPs in the PSCLC that is likely responsible for the AuNP arch formation that mimics the arches of the PSCLC top layer, we superimposed contrasted PLM and SEM images in Figure 2e. The orientation of the stripes evolved from 0° to 90° relative to the polarizer direction. The polarizer was aligned at 6° (see Supplementary Information, Figure S4) to the rubbing direction. Between crossed polarizers, these curved stripes, for sufficiently gentle curvatures that do not alter the CLC structure, can be understood as straight stripes with a varying orientation relative to the crossed polarizers: The orientation of the stripes along Zone 1 in Figure 2e is equivalent to the 0° orientation of Figure 1e, where the stripes are parallel to the polarizer. Here, the AuNPs deposit along the bright region of the stripe. As in the case of 45°, the stripes in Zone 3 exhibit a narrow dark center surrounded by bright regions, with AuNPs visible in this narrow dark area. The stripes in Zone 5 correspond to a 90° rotation, and the AuNPs are again aligned along the central bright region. Zones 2 and 4 are intermediate regions where

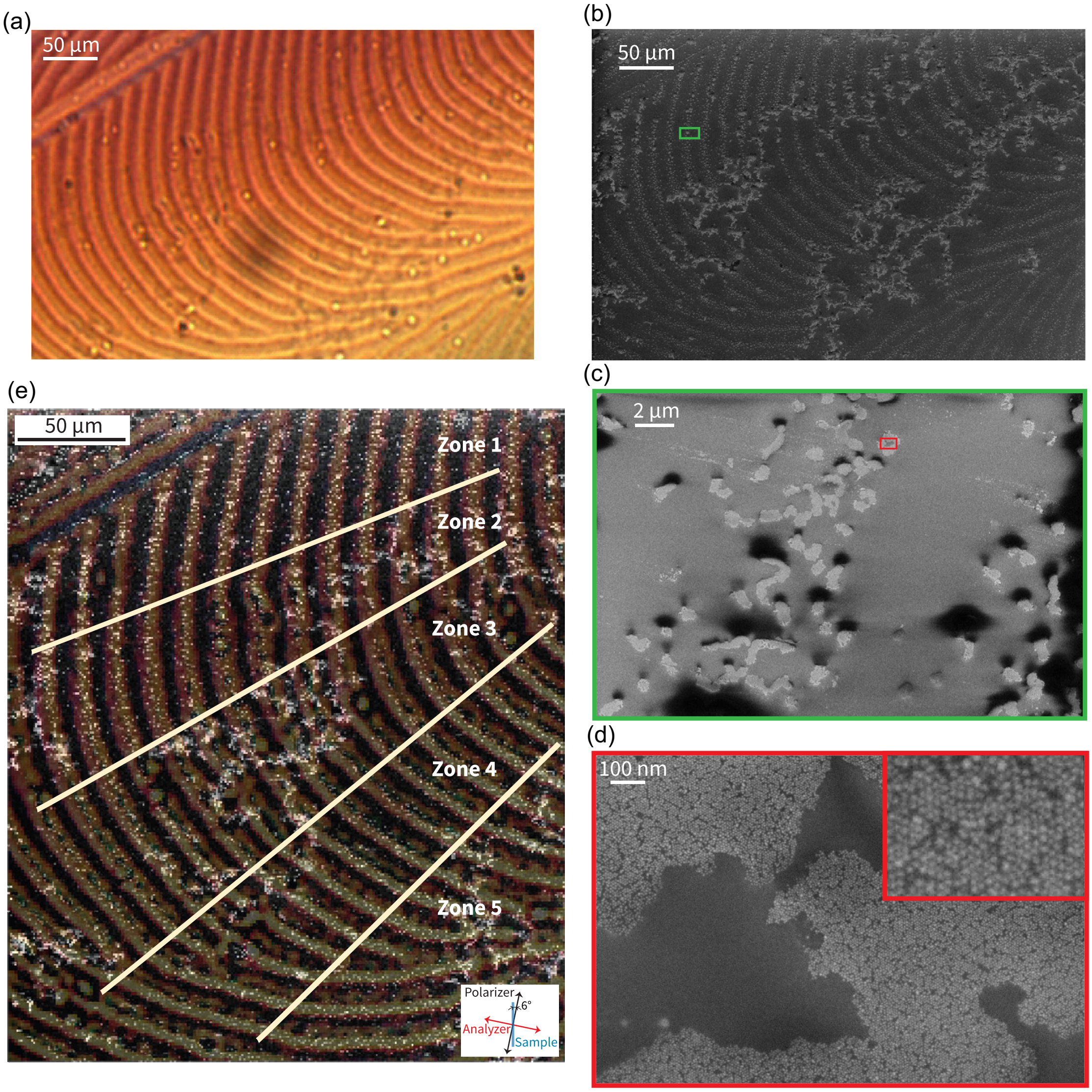

FIGURE 2 | (a) Cross-polarized transmission optical microscopy image of a PSCLC-AuNPs film. (b) SEM image showing self-organization into gold nanoparticle fibers (in white) that follow the cholesteric modulation. (c) Magnified SEM image of AuNP fiber-like features within the undulations, showing their clustering into islands. (d) Enlargement according to the red frame in (c) showing monolayered islands of AuNPs; an inset showing their local organization. (e) Contrasted and superimposed PLM and SEM images highlighting the PLM stripes and the AuNP arches, which follow the pattern of the cholesteric surface. The PLM image (a) was taken between crossed polarizers, with the polarizer at 6° relative to the rubbing direction. This angle corresponds to the mean orientation of the stripes in Zone 1. In Zone 3, a higher density of AuNPs is observed, corresponding to defects in the stripes as underlined in Figure S5, where the cholesteric stripes misalign.

the AuNPs undergo a progressive transition following the continuous rotation of the stripes. Figure 2e shows that the AuNPs rotate with the stripes and precisely follow a well-defined specific region of the cholesteric texture. The notably higher density of AuNPs observed in Zone 3 can be attributed to the presence of topological defects in the PSCLC within that region, which are known to attract and confine AuNPs (see Figure S5).

To obtain even more information about the localization of AuNPs, AFM images of the PSCLC-AuNPs surface were obtained. The PSCLC-AuNPs films feature undulations (Figure 3a,e) similar to those observed in PSCLC films without AuNPs (Figure 1c,d). Although the undulation period Λ was similar to the one without AuNPs, the peak-to-valley distance increased by 25% following AuNP deposition. By AFM, we indeed measured $\Lambda = 17.2 \pm 0.2\,\mu\text{m}$ (80 measurements) and an average peak-to-valley distance of $100.5 \pm 10.0\,\text{nm}$. At the bottom of the valleys in the AFM topography image (Figure 3a,c), the same islets as imaged by SEM are observed. The fact that they are composed of AuNPs is supported by a local increase in AFM phase exclusively at the level of the islands (Figure 3b). It was also observed that systematically these islands induce the formation of depressions at the PSCLC/air interface that cause an increase in the average peak-to-valley distance (Figure 3a,c,d). The depth of these depressions, measured by AFM (Figure 3d) over 164 islets, is of average value 20.4 nm, with a small dispersity of ±0.3 nm.

On the three undulation periods shown in Figure 3a, we performed 37 height profile measurements to obtain the average localization of the AuNP depressions. The average of the 37 profiles is plotted in blue in Figure 3e. It shows that the average

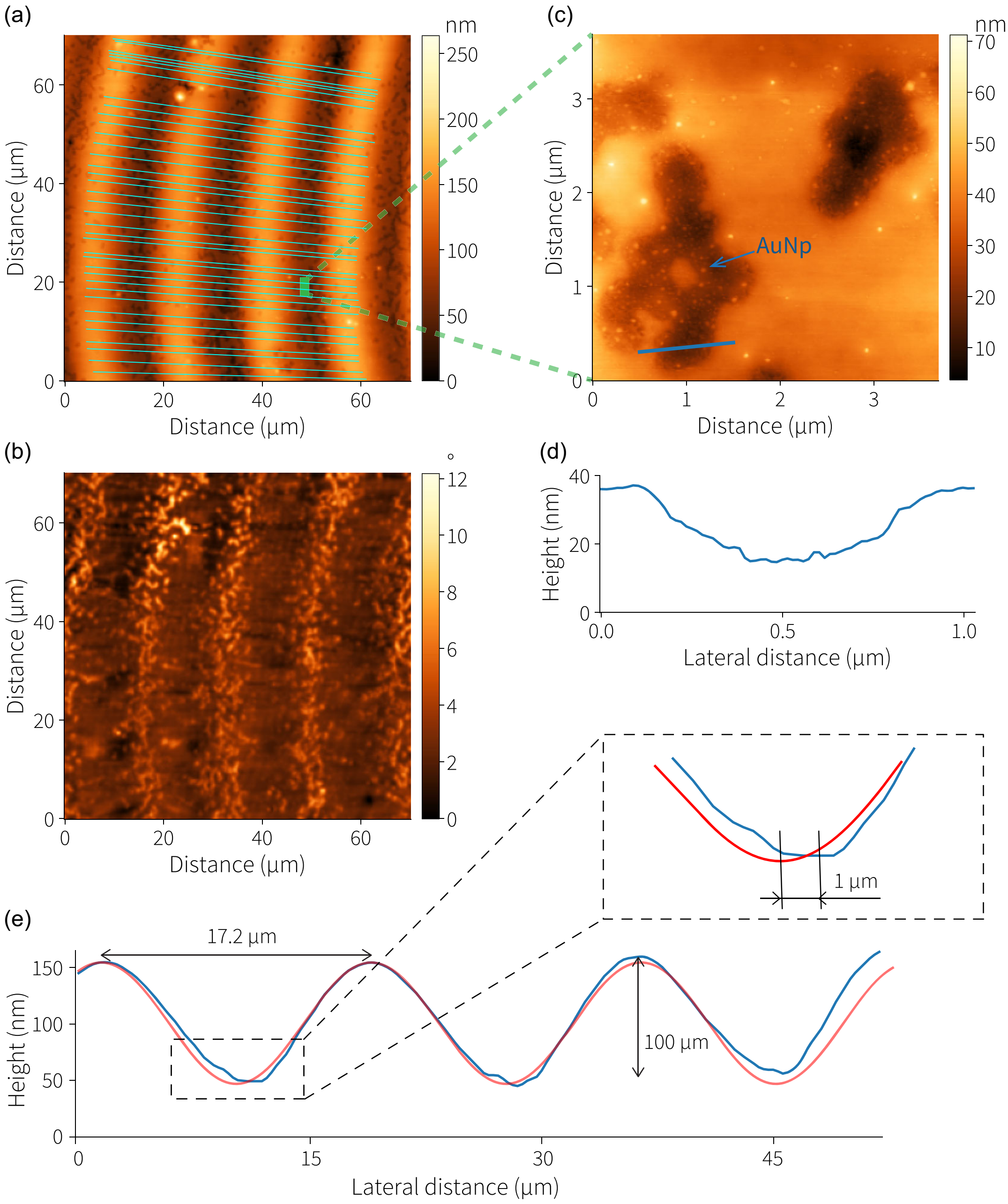

FIGURE 3 | AFM images of the topography (a,c) and phase (b) of a PSCLC-AuNPs film. The region in the green rectangle of (a) is imaged in (c), which shows islets of AuNP carving out the cholesteric surface. (e) and (d) are height profiles along the directions marked in (a) and (c), respectively. The height profile in blue in (e) is an average of 37 profiles shown above (in (a)). The trace in red is a sine curve. The enlarged region in the valley shows a shift of 1µm in the localization of AuNPs with respect to the valley base.

localization of the AuNP depressions is slightly shifted with respect to the center of the undulations, which is determined by comparing it to a sine curve of similar period (red curve in Figure 3e). The average shift was around 1 µm, 5% of the undulation period. Being averaged over a very large number of depressions shown in Figure 3a, this shift is small but significant. It appears to be in the same direction for the three periods, but it is likely not the case for all the arches.

We conclude that AuNPs organize within arches because of their preferential localization in the valleys of the top modulated layers of the PSCLC films. The precise localization of AuNPs is slightly below the PSCLC/air interface, leading to a depression of 20 nm. The preferential region for AuNPs revealed by PLM, SEM, and AFM measurements corresponded to the valleys of the surface undulations of the top layers, but with a small shift of about 5% with respect to the center of the valley.

2.3 | Cholesteric Film Interface: Energy Considerations

To understand why AuNPs assemble in monolayers that mimic the cholesteric modulation, we investigated the CLC structure and energetics for a ratio between thickness and pitch mimicking the experimental one equal to 1.5 (see the

Section 4). We simulated a cholesteric system between planar and homeotropic anchoring with constant pitch and undulation period and minimized the Landau-de Gennes free energy density [44] as described in the Section 4. Figure 4a shows the corresponding configuration of director $\mathbf{n}$ (gray cylinders). Close to the substrate, we recover a planar structure with the cholesteric pitch perpendicular to the substrate that tilts close to the air interface to become parallel to the air interface (Figure 4a). There, the disruption of the preferred cholesteric twist leads to elastic deformations that are quite pronounced at the air interface, particularly in the hills and valleys (Figure 4a). If we anticipate that in PSCLC the AuNP structure is not modified by the polymerization that comes after AuNP assembly in the CLC film, this result suggests that the preferred localization for AuNPs should be close to the air interface in the hills or in the valleys. AuNP monolayers would then take the place of the most distorted areas, saving a significant amount of cholesteric elastic energy.

In order to understand why valleys are preferred for the localization of AuNPs with respect to hills, it is useful to recall the anchoring properties of the AuNP monolayers. Using nematic 5CB, without chiral dopants, it has been shown that anchoring below the monolayers of the same AuNPs is tilted and neither perfectly planar nor homeotropic [18]. The color map which depicts the magnitude of the angle between the director $\mathbf{n}$ and the vertical direction $\hat{\mathbf{z}}$ in Figure 4c shows that, according to simulations, the molecules are generally homeotropic along the sinusoidal interface, except at the peaks and valleys. The pitch defects at the extrema cause the director to turn and become perpendicular to the vertical direction. This reorientation is more rapid in the peaks than in the valleys. The smoother variation in the valleys creates larger regions of tilted director orientations away from the homeotropic direction. The conical anchoring energy [45] density $\overline{W_a}$ at the sinusoidal interface was computed for different possibilities of easy axis tilt angles between 0° and 35°.

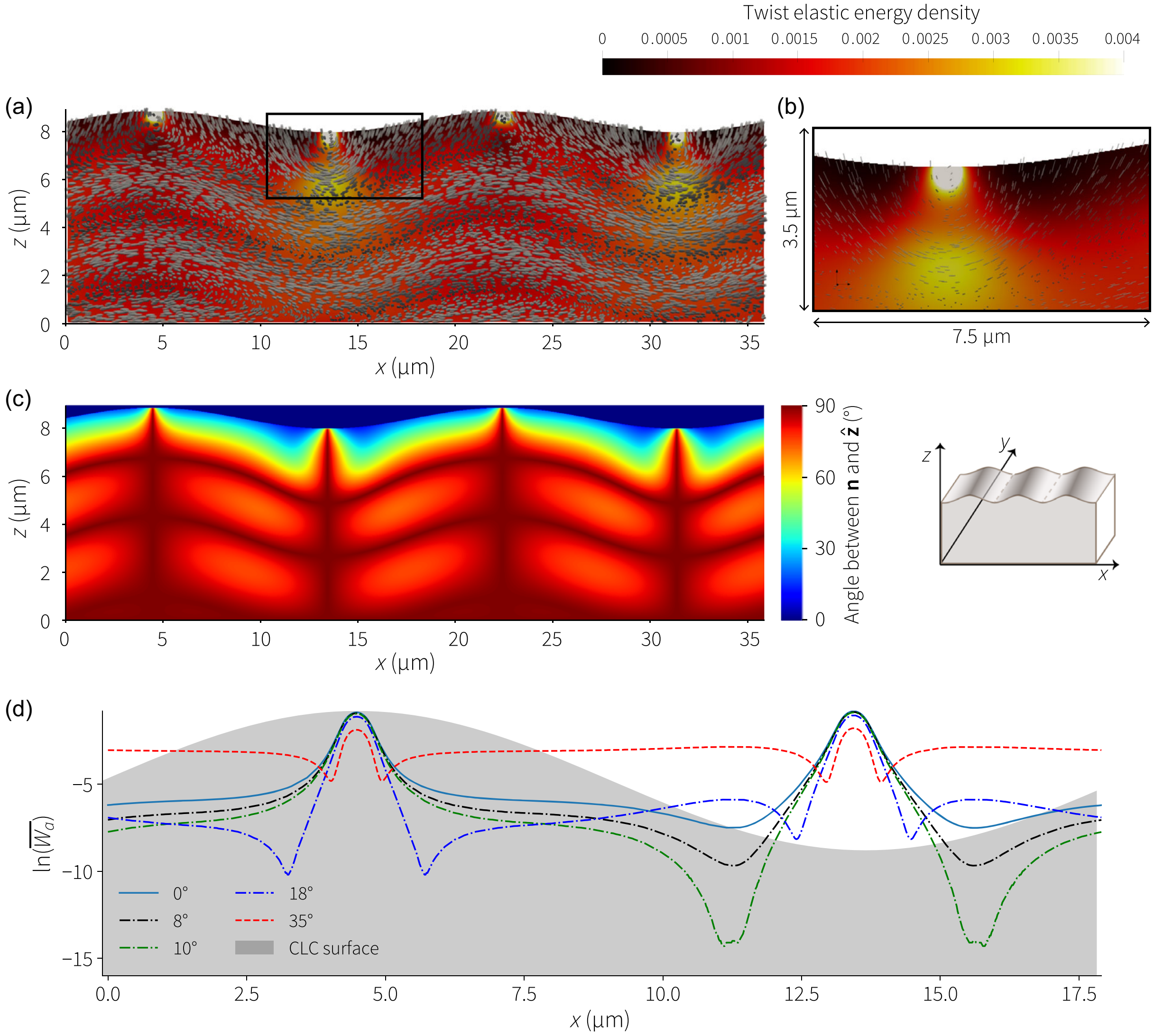

FIGURE 4 | (a) Configuration of $\mathbf{n}$ (gray cylinders) obtained by minimizing Landau-de Gennes free energy density in the CLC elastic layer. The color depicts the twist elastic energy density, which varies mainly due to disruption in the preferred cholesteric twist. (b) Elastic distortions in the magnified boxed valley region of (a). (c) Color map of the angle between the $\mathbf{n}$ and $\hat{\mathbf{z}}$ (vertical direction as shown in the right image, which displays the sample and axes). (d) Logarithm of the averaged dimensionless anchoring energy density $\overline{W_a}$ at different tilt angles, plotted along the sinusoidal surface shaded in gray.

We found that for small tilt angles less than 20°, the average anchoring energy density could become particularly low near the valleys (Figure 4d). In particular, Figure 4d shows that for a tilt of 10°, a narrow zone of significantly smaller anchoring energy is observed at 2 μm from the valley center (in red in Figure 4d). This result is consistent with AFM results (Figure 3e) that lead to an average localization of the AuNP monolayers at around 1 μm from the valley center. The experimentally observed localization could be even closer to the valley center, which can be explained as the effect of elastic energy, which is largest at the valley center exactly (Figure 4b). Moreover, the presence of the monomer likely influences the anchoring on AuNP monolayers, which could also contribute to the slight difference observed between the experimental AFM results for AuNP localization (around 1 μm) and the simulation analysis (around 2 μm). Thus, the balance between anchoring and elastic energies localizes the AuNP monolayers just near, but not exactly in, the valley center. A small variation of this localization should be induced by CLC thickness variation, as it is known that the superstructure period increases with the ratio of thickness over pitch [41]. The period increase is at most 40% when the thickness over pitch ratio increases over fivefold, from 1.5 to 8. Even with a thickness over pitch ratio of 8, we do not expect the AuNP to shift away from the valley center by much more than 0.8 micrometers.

We found through AFM measurements (Figure 3e,d) that the AuNPs were placed about 20 nm deep in the CLC. This suggests that the optimal balance between anchoring energy and elastic energy even imposes a localization slightly below the air interface despite the induced line tension around the corresponding depressions (Figure 3c). It remains unclear why in Figure 3e mostly one side is filled by AuNPs instead of the two symmetric sides around the valley center. It is possible that once AuNPs start to fill one of the two sides, the CLC-modulated top layer becomes slightly distorted and asymmetric, which would favor this side mostly. Such a distortion is indeed suggested close to the bottom of the undulations in the surface profiles in the presence of AuNPs shown in Figure 3e.

An easy axis tilted by 10° below the AuNP monolayers is less tilted than the tilted easy axis observed at a nematic-air interface. We have indeed measured the anchoring characteristics below AuNP monolayers on top of polymer-stabilized nematic liquid crystal (PSNLC) films, leading to a range from 17° to 39° depending on the model that was used to calculate the effective birefringence [18]. Figure 4d shows that if the anchoring easy axis tilt was increased to 18°, the corresponding anchoring energy on CLC would be less favorable. The imposed localization of AuNP monolayers on top of the modulated cholesteric top layer thus, might induce a less tilted anchoring with respect to the one that is observed on top of the PSNLC. Using SEM, we have compared the local AuNP monolayers after polymerization between the one formed on top of nematic films and the one on top of the cholesteric modulated top layer (Figure 5). We systematically observe that the hexagonal order of the AuNP monolayer is not so well-defined at the CLC surface (Figure 5b) compared to the nematic surface (Figure 5a).

We calculated the global sixfold orientational order Q_6 (see Section 4) after extracting the AuNP positions from SEM images, as shown by circles overlayed on SEM images in Figure 5 [46]. AuNPs on PSNLC showed $Q_6 = 0.15 \pm 0.03$ (17 images), whereas on PSCLC, we noted $Q_6 = 0.04 \pm 0.02$ (6 images). While AuNPs on PSNLC show some hexagonal arrangement, they are disordered on PSCLC as their global order is closer to a simulated distribution of random particles on similarly sized images ($Q_6^{\mathrm{rnd}} = 0.01 \pm 0.00$). The disorder on PSCLC-AuNPs can be because its modulated top layer not only allows for the formation of AuNP arches that mimic the modulated structure, but it also

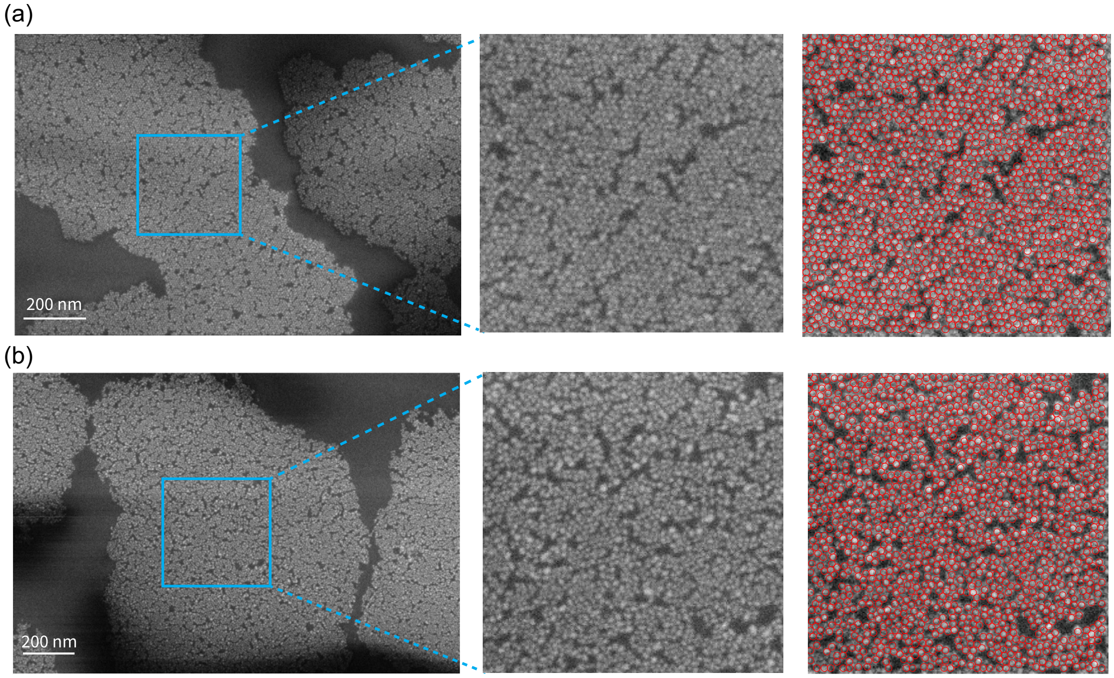

FIGURE 5 | SEM images showing the arrangement of the AuNP monolayer on the PSNLC (a) and PSCLC (b). The zoomed regions (a) and (b) showing the local geometric structure formed by the AuNPs, and the images to their right show AuNP selection using overlayed circles in red, which were used to calculate the hexagonal disorder.

has a local impact: The imposed nonoptimal easy-axis anchoring tilt deteriorates the quality of the AuNP order within the hexagonal AuNP monolayers.

We believe that the fact that a subtle balance between elastic energies and anchoring energies not only determines the large-scale architecture of the AuNP monolayers but also influences the nanoscale packing within the monolayers. It could be a general characteristic of these composites in which liquid crystal modulated superstructures impose a specific assembly of nanoparticles. These composites are promising for their possible tunability of the nanoparticle properties related to the liquid crystal character of the matrix; it is important now to understand them in depth. For example, we can consider the nanoparticle–cholesteric composites stabilized by vitrification with modulated superstructure induced by degenerate planar anchoring on the substrate (cholesteric fingerprints) [24]. It has been suggested that the nanoparticles were on the top of the modulation in contrast with the AuNP monolayers localized with a small but clear shift with respect to the valley centers in our photopolymerizable system with unidirectional planar anchoring [24]. It would be interesting to understand if this is due to differences in anchoring energies of the two kinds of nanoparticles with respectively octanethiol and dodecanethiol ligands or due to differences in the structures of the two modulated superstructures.

We plan in future experiments to measure the evolution of AuNP monolayer localization and internal structure when AuNP concentration vary with the idea that new structures of AuNPs could emerge for new interesting plasmonic or catalytic properties. A new article on the influence of AuNP concentration is in preparation.

3 | Conclusion

Using various imaging techniques, including AFM, SEM, and PLM, in combination with simulation, we have established that AuNP monolayers localize in the valleys of an undulated cholesteric modulated superstructure at the air interface. The localization is slightly displaced by around 1 μm with respect to the valley centers, partially mitigating the large elastic energy found near the pitch axis defects in the valleys and hills while satisfying a tilted anchoring at the AuNP monolayer. This shows that both elastic considerations and anchoring properties at the AuNP monolayer surface play an important role in establishing the preferred monolayer location. Moreover, the simulations show that the optimum easy axis for the AuNP monolayer at the CLC surface is of the order of 10°, smaller than the one between 17 and 39° at the nematic surface. The observed local disorder of the AuNP monolayer assembly, more disordered than the corresponding assemblies at the nematic surface, is consequently the result of the imposed lower tilt of the easy axis characterizing the anchoring at the AuNP monolayer at the CLC surface. We finally demonstrate how elasticity and anchoring control the AuNP monolayer structure at all scales, from the large scales where large arches are formed to the nanoscopic scale where a disorder in the AuNP assembly is induced.

In the future, it will thus be interesting to study how the AuNP assemblies will react to external stimuli for an active tuning of the plasmonic properties of the AuNP monolayers. We will study whether the arches remain stabilized by the polymerized architecture or can be reversibly tuned at the cholesteric/nematic transition. Even if the arches are stabilized, we expect the local interaction associated with the anchoring energy to vary at the cholesteric/nematic transition, with a possible reversible variation in the local monolayer structure that might allow for a tuning of the plasmonic absorption of the AuNP assemblies. We already successfully removed the polymerized film from its substrate and demonstrated that the arch structure remains unmodified. This opens the door to the possibility of actively and reversibly tuning the plasmonic properties of AuNPs through a large number of stimuli, like stretching of the polymer matrix or presence of solvent. This latter one has been shown to induce reversible mechanical deformations of the polymer matrix, such as curling [47].

4 | Methods

4.1 | Substrate Preparation

Clean glass slides were spin-coated with polyvinyl alcohol (PVA) and baked for 1 h at 120°C for polymerization and simultaneously rubbed unidirectionally to promote planar anchoring at the surface of CLC and PSCLC samples. For SEM analysis of PSCLC samples, the glass slide was coated with a thin layer of indium tin oxide for charge dissipation.

4.1.1 | CLC Mixture

CLCs were prepared by doping 2 wt% of chiral agent S-2011 (MLC-6247, Merck) in the nematic liquid crystals (NLCs) 4-pentyl-4′-cyanobiphenyl (5CB, Sigma–Aldrich). This resulted in a helical pitch p = 5.5 μm (measured with the Grandjean-Cano wedge method). 5CB was in the nematic phase from 18°C to 35°C, and with high optical anisotropy $\Delta n = n_e - n_o$, where $n_e = 1.72$ is the extraordinary index (parallel to the optical axis) and $n_o = 1.54$ is the ordinary index (perpendicular to the optical axis).

4.1.2 | Photopolymerizable Monomer−CLC Mixture

CLC mixture was mixed with a monomer RM257 (30 wt% Synthon Chemicals GmbH & Co. KG) and a photo-initiator (1-hydroxycyclohexyl phenyl ketone, 1.2 wt%, Sigma–Aldrich), to which dichloromethane was added to promote miscibility. This LC monomer mixture was heated at 60°C for 45 minutes in a closed flask, where dichloromethane was in the gas phase. Then the flask was opened to evaporate the dichloromethane and obtain a homogeneous LC monomer mixture. The main idea of our mixture is to stabilize the alignment of a low molecular weight LC through elastic interactions between the polymer network and the LC. This mixture ultimately produces polymer-stabilized cholesteric liquid crystals, which we call PSCLC.

4.1.3 | AuNP Synthesis

50 mg of $HAuCL_4$ (98%, Sigma–Aldrich) was mixed with 5 ml of oleylamine (70%, Sigma–Aldrich) and 5 ml of tetralin (1,2,3,4-tetrahydronaphthalene, 99% Sigma–Aldrich) in a three-neck flask and degassed at room temperature. The flask was then placed in an ice bath with a temperature controller. A mixture of 22 mg of tert-butyl-amine borane (97%, Strem), 0.5 ml of oleylamine, and 0.5 ml of tetralin was prepared and sonicated till the salt completely dissolved. The three-neck flask was placed in an Ar

environment, and borane solution was injected promptly, which changed the color of the solution to brown and then to purple. After 36 min, 0.5 ml of DDT (1-dodecanethiol, ≥98% Sigma–Aldrich) was added to stop the reaction. 5 ml of ethanol (99.85%, VWR Chemicals) was added, and the flask was centrifuged to separate the AuNPs, which were redispersed in toluene (98%, Riedel-de Haën). In this way, 6 nm diameter AuNPs surrounded by DDT ligands with a polydispersity of 9% were obtained. The small angle X-ray scattering (SAXS) measurements for AuNP diameter determination were carried out at the Soleil synchrotron.

4.1.4 | CLC and PSCLC Film Preparation With or Without AuNPs

10 μl of cholesteric material was spin-coated at 2000 rpm for 20 s on PVA-coated glass slides to generate a uniform hybrid film, with planar anchoring on the PVA substrate and homeotropic anchoring at the cholesteric–air interface. Optical microscopy and profilometer scanning were used to check film thickness. The imaged PSCLC film was 10μm thick, and using the relations given by the experimental and theoretical study [41], we find the helical pitch $p = 6.7$ μm. Polymerization increased the CLC pitch (5.5 μm) by 1.2 μm. The addition of a monomer reduces the concentration of the chiral dopant in the CLC, which increases its helical pitch [48]. AuNPs were deposited on the CLC by drop casting the AuNP solution ($5.6 \times 10^{17}\,\mathrm{L}^{-1}$). The samples were polymerized by UV light irradiation (365 nm, 0.15 mW/cm [2]) in a nitrogen atmosphere for 20 min at room temperature [18, 26, 27].

4.2 | Sample Characterization

4.2.1 | Polarized Light Microscopy (PLM)

The samples were observed with a Leica DMRX optical microscope that included a charge-coupled device (CCD) camera. Broadband light from a xenon lamp was passed through a polarizer and used to illuminate the sample. The polarizer was oriented at 0° to the rubbing direction on the sample. The light through the sample was further transmitted through an analyzer oriented at 90° to the sample. To monitor the intensity of PSCLC stripes at different angles, the sample was rotated between crossed polarizers.

4.2.2 | Atomic Force Microscopy (AFM)

A Veeco Dimension 3100 AFM operating in tapping mode with a Bruker cantilever and tip (500 kHz) was used to image PSCLC films with and without AuNPs.

4.2.3 | Scanning Electron Microscopy (SEM)

The Zeiss SUPRA 40 SEM was used to image the PSCLC films with AuNPs.

4.3 | Cholesteric Free Interface Simulation

The nematic configuration at the free interface was found by minimizing the Landau-de Gennes free energy density (in dimensionless units)

$$f_{\mathrm{LdG}} = -\frac{1}{2}\mathrm{tr}(\mathbf{Q}^2) - \frac{\mathrm{B}}{3}\mathrm{tr}(\mathbf{Q}^3) + \frac{\mathrm{C}}{4}[\mathrm{tr}(\mathbf{Q}^2)]^2 + \frac{\mathrm{L}_1}{2}(\nabla \times \mathbf{Q} + 2\mathrm{q}_0\mathbf{Q})^2 + \frac{\mathrm{L}_2}{2}(\nabla \cdot \mathbf{Q})^2 \tag{1}$$

where Q is the symmetric, traceless 3×3 matrix order parameter. The B and C coefficients set the thermodynamic potential, and $L_{1,2}$ fixes the elastic distortion free energy cost. Since we know the cholesteric forms parallel layers deep in the bulk of the sample, we chose a uniform cholesteric with the pitch along the $\hat{z}$ direction (Figure 4c) as our initial configuration with

$$Q = \frac{3S_0}{4}\begin{pmatrix} \cos\,(2q_0 z) + \frac{1}{3} & \sin\,(2q_0 z) & 0 \\ \sin\,(2q_0 z) & \frac{1}{3} - \cos\,(2q_0 z) & 0 \\ 0 & 0 & -\frac{2}{3} \end{pmatrix} \tag{2}$$

where $S_0 = 0.533$ is the preferred scalar order parameter (set by choosing $\mathrm{B} = 12.3256$ and $\mathrm{C} = 10.0581$ in Equation (4), and $P_0 = 2\pi/q_0$ is the cholesteric pitch).

The energy was minimized on a cubic lattice with spacing $\Delta x = 0.0175\,\mu\mathrm{m}$. Although it was possible to simulate a free interface by, for example, introducing a coexisting isotropic phase above the cholesteric, here we opted to create a fixed sinusoidal interface with a specified geometry and anchoring strength. We assumed that the stripes were uniform along the $\hat{y}$ direction, and we simulated an effectively two-dimensional system with a width of $L_x = 2048\Delta x \approx 35.8\,\mu\mathrm{m}$ and a sinusoidal height (along $\hat{z}$ direction) $h(x) = h_0 + A\sin(2\pi x/\lambda_A)$, where $h_0 = 480\Delta x \approx 8.4\,\mu\mathrm{m}$ is the midline height, $A = 25\Delta x \approx 0.438\,\mu\mathrm{m}$ is the amplitude, and $\lambda_A = 1024\Delta x \approx 17.9\,\mu\mathrm{m}$ is the period to accommodate two full undulations in our simulation box. By selecting $q_0 = 0.02\Delta x^{-1}$, we obtained a cholesteric pitch of $P_0 \approx 5.50\,\mu\mathrm{m}$. These parameters are consistent with experimental measurements of the surface undulations and the cholesteric pitch. We used a two-constant approximation in which the splay and bend elastic constants were equal, $K_1 = K_3 \approx 10$ pN and the twist constant $K_2 \approx 5$ pN. These values correspond to $L_1 = 0.7425$ and $L_2 = 0.22275$ in our dimensionless free energy density above.

At the sinusoidal surface, we imposed a homeotropic anchoring via a Rapini-Papoular potential with surface density

$$f_{\mathrm{W}} = \mathrm{W}_0\mathrm{tr}[(\mathrm{Q} - \mathrm{Q}_{\mathrm{B}})^2] \tag{3}$$

where $Q_B = \frac{3}{2}S_0\left(n_i n_j - \frac{1}{3}\delta_{ij}\right)$ is the uniaxial tensor associated with the surface normal n. We set $W_0 = 0.004$, corresponding to an anchoring strength of $3.1 \times 10^{-5}\,\mathrm{J/m^2}$. Strong degenerate planar anchoring was enforced at the bottom of the sample to force the cholesteric pitch axis to be parallel to $\hat{z}$ at the bottom. The minimization was performed using the conjugate gradients method [44], provided in the ALGLIB numerical analysis package.

The Landau-de Gennes free energy density f_{LdG} was minimized using the calculated Q-tensor to find the director $\mathbf{n}$ configuration. At each lattice site, the twist elastic energy density was estimated as

$$f_{\mathrm{e}} = \mathrm{S}_0^{-2}(\nabla \times \mathbf{Q} + 2\mathrm{q}_0\mathbf{Q})^2 \tag{4}$$

The canonical anchoring energy density W_a at the sinusoidal surface was estimated using the modified Fournier-Galatola potential [45]

$$W_a = \left[\nu_i \nu_k \widetilde{Q}_{kl} \nu_l \nu_j - \tfrac{3}{2} S_0 \cos^2 \alpha\, \nu_i \nu_j\right]^2 \tag{5}$$

where ν_i are components of the surface normal ν, $\widetilde{Q_{ij}} = Q_{ij} + \frac{1}{2} S_0 \delta_{ij}$, and tilt angle α is the preferred angle between ν and n. The averaged anchoring energy density $\overline{W_a}$ was found by averaging W_a over a disk of radius $15\Delta x$ along the sinusoidal surface, for which $\nu = (\lambda_A^2 + [2\pi A \cos\,(2\pi x/\lambda_A)]^2)^{-1/2}[\lambda_A \widehat{z} + 2\pi A \cos\,(2\pi x/\lambda_A)\widehat{x}]$.

4.4 | Sixfold Orientational Order

The order in AuNP monolayers on polymer-stabilized LC substrates was estimated by finding the position of AuNP centers in SEM images and computing the order magnitude. The local sixfold bond-orientational order parameter for the particle j is defined as [46, 49]

$$\psi_{6,j} = \frac{1}{n} \sum_{k=1}^{n} e^{\imath 6 \theta_{jk}} \tag{6}$$

where n is the number of nearest neighbors and θ_{jk} is the angle of the bond connecting particle j to neighbor k. The magnitude $|\psi_{6,j}|$ is the degree of local sixfold symmetry: $|\psi_{6,j}| = 1$ for a perfect hexagonal arrangement, and $|\psi_{6,j}| = 0$ denotes a complete lack of hexagonal orientation order. The global order parameter Q_6 estimates the global sixfold orientational order by averaging over of all N considered particles in a region [46]

$$Q_6 = \frac{1}{N} \left| \sum_{j}^{N} \psi_{6,j} \right| \tag{7}$$

Author Contributions

Ines Gharbi prepared the samples and performed optical, atomic, and electronic microscopy characterization and analysis. **Amit R. Dhawan** analyzed and modeled microscopy data and nanoparticle distribution. **Maxim O. Lavrrentovich** modeled the cholesteric interface and simulated the structure. **Randall D. Kamien** investigated microscopy and simulation results. **Emmanuelle Lacaze** designed and supervised the project and investigated the data. **Ines Gharbi**, **Amit R. Dhawan**, and **Emmanuelle Lacaze** wrote the manuscript. All authors discussed the results and edited the manuscript.

Acknowledgments

I.G. was supported by the Tunisian Ministry for Higher Education, Research, and Technology and by the CNRS-UMR7588. I.G.'s travel between Tunis and Paris was supported by a grant from Université de Tunis El Manar and, more specifically, from the LR99ES16. A.R.D. thanks Tristan Farrow for the discussions.

Funding

This work was supported by Université de Tunis El Manar, Centre National de la Recherche Scientifique (Grant UMR7588).

Conflicts of Interest

The authors declare no conflicts of interest.

Data Availability Statement

The data that support the findings of this study are available from the corresponding author upon reasonable request.

References

1. P. Oswald and P. Pieranski, *Nematic and Cholesteric Liquid Crystals: Concepts and Physical Properties Illustrated by Experiments* (CRC press, 2005).
2. I.-C. Khoo, *Liquid Crystals* (John Wiley & Sons, 2022).
3. Z. Wang, T. Xu, A. Noel, Y.-C. Chen, and T. Liu, "Applications of Liquid Crystals in Biosensing," *Soft Matter* 17 (2021): 4675–4702.
4. K. Yin, E.-L. Hsiang, J. Zou, et al., "Advanced Liquid Crystal Devices for Augmented Reality and Virtual Reality Displays: Principles and Applications," *Light: Science & Applications* 11 (2022): 161.
5. E. Lüder, P. M. Knoll, and S. H. Lee, *Liquid Crystal Displays: Addressing Schemes and Electro-Optical Effects* (John Wiley & Sons, 2022).
6. F. Reinitzer, "Contributions to the Knowledge of Cholesterol," *Liquid Crystals* 5 (1989): 7–18.
7. J. Uchida, B. Soberats, M. Gupta, and T. Kato, "Advanced Functional Liquid Crystals," *Advanced Materials* 34 (2022): 2109063.
8. T. Kato, J. Uchida, T. Ichikawa, and T. Sakamoto, "Functional Liquid Crystals: Towards the Next Generation of Materials," *Angewandte Chemie International Edition* 57 (2018): 4355–4371.
9. J. P. F. Lagerwall and G. Scalia, "Series in Soft Condensed Matter," *Liquid Crystals with Nano and Microparticles: (In 2 Volumes). Series in Soft Condensed Matter* (World Scientific, 2016), https://doi.org/10.1142/9280.
10. C. Blanc, D. Coursault, and E. Lacaze, "Ordering Nano-and Microparticles Assemblies with Liquid Crystals," *Liquid Crystals Reviews* 1 (2013): 83–109.
11. D. Coursault, J. Grand, B. Zappone, et al., "Linear Self-Assembly of Nanoparticles Within Liquid Crystal Defect Arrays," *Advanced Materials* 24 (2012): 1461–1465.
12. S. P. Do, A. Missaoui, A. Coati, et al., "From Chains to Monolayers: Nanoparticle Assembly Driven by Smectic Topological Defects," *Nano Letters* 20 (2020): 1598–1606.
13. J. Milette, S. J. Cowling, V. Toader, et al., "Reversible Long Range Network Formation in Gold Nanoparticle - Nematic Liquid Crystal Composites," *Soft Matter* 8 (2012): 173–179.
14. S. P. Do, A. Missaoui, A. Coati, et al., "Interactions Between Topological Defects and Nanoparticles," *Frontiers in Physics* 7 (2020): 234.
15. H. Jeridi, J. de Dieu Niyonzima, C. Sakr, et al., "Unique Orientation of 1D and 2D Nanoparticle Assemblies Confined in Smectic Topological Defects," *Soft Matter* 18 (2022): 4792–4802.
16. W. Lewandowski, T. Łojewska, P. Szustakiewicz, J. Mieczkowski, and D. Pociecha, "Reversible Switching of Structural and Plasmonic Properties of Liquid-Crystalline Gold Nanoparticle Assemblies," *Nanoscale* 8 (2016): 2656–2663.
17. C. N. Mahyaoui, C. E. Goldmann, E. Garre, et al., "Nanoparticles Confined in Liquid Crystalline Coatings with Smectic Focal-Conic Textures: Implications for Precise Nanoparticle Positioning," *ACS Applied Nano Materials* 8 (2025): 5207–5217.
18. I. Gharbi, V. Palacio-Betancur, H. Ayeb, et al., "Liquid Crystal Films as Active Substrates for Nanoparticle Control," *ACS Applied Nano Materials* 4 (2021): 6700–6708.

19. H. Jeridi, S. Royer, E. Lhuillier, and E. Lacaze, “Temperature-Activated Polarization of Single Photon Emitters,” *Applied Physics Letters* 123 (2023): 203101.

20. E. Lee, Y. Xia, R. C. Ferrier Jr., et al., “Fine Golden Rings: Tunable Surface Plasmon Resonance from Assembled Nanorods in Topological Defects of Liquid Crystals,” *Advanced Materials* 28 (2016): 2731–2736.

21. M. Mitov, C. Portet, C. Bourgerette, E. Snoeck, and M. Verelst, “Long-Range Structuring of Nanoparticles by Mimicry of a Cholesteric Liquid Crystal,” *Nature Materials* 1 (2002): 229–231.

22. M. Mitov, C. Bourgerette, and F. Guerville, “Fingerprint Patterning of Solid Nanoparticles Embedded in a Cholesteric Liquid Crystal,” *Journal of Physics: Condensed Matter* 16, no. 19 (2004): S1981.

23. M. Mitov, F. Guerville, and C. Bourgerette, “Evidence of Surface Segregation in the Organization of Metallic Nanoparticles Dispersed in a Cholesteric Liquid Crystal,” *Molecular Crystals and Liquid Crystals* 435 (2005): 13–673.

24. R. Bitar, G. Agez, and M. Mitov, “Cholesteric Liquid Crystal Self-Organization of Gold Nanoparticles,” *Soft Matter* 7 (2011): 8198–8206.

25. J. S. Evans, P. J. Ackerman, D. J. Broer, J. van de Lagemaat, and I. I. Smalyukh, “Optical Generation, Templating, and Polymerization of Three-Dimensional Arrays of Liquid-Crystal Defects Decorated by Plasmonic Nanoparticles,” *Physical Review E* 87 (2013): 032503.

26. I. Dierking, “Polymer Network–stabilized Liquid Crystals,” *Advanced Materials* 12 (2000): 167–181.

27. I. Gharbi, A. Missaoui, D. Demaille, E. Lacaze, and C. Rosenblatt, “Persistence of Smectic-A Oily Streaks into the Nematic Phase by UV Irradiation of Reactive Mesogens,” *Crystals* 7 (2017): 358.

28. Y. Ye, L. Guo, and T. Zhong, “A Review of Developments in Polymer Stabilized Liquid Crystals,” *Polymers* 15 (2023): 2962.

29. A. Gridyakina, N. Kasian, M. S. Chychłowski, M. Kajkowska, and P. Lesiak, “Advances in Multicomponent Systems: Liquid Crystal/Nanoparticles/Polymer,” *Materials Today Physics* 38 (2023): 101258.

30. A. Gruzdenko and I. Dierking, “Electro-Optic Properties of Polystyrene Particle-Laden Polymer-Stabilized Liquid Crystals,” *Journal of Materials Chemistry C* 11 (2023): 5438–5449.

31. M. Roohnikan, V. Toader, A. Rey, and L. Reven, ”Hydrogen-Bonded Liquid Crystal Nanocomposites,“ *Langmuir* 32 (2016): 8442–8450.

32. M. Roohnikan, M. Lindner-D’Addario, V. Toader, et al., “Mechanochemical Nanoparticle Functionalization for Liquid Crystal Nanocomposites Based on COOH-Pyridine Heterosynthons,” *Journal of Materials Chemistry C* 6 (2018): 1789–1796.

33. B. Senyuk, C. Meng, and I. I. Smalyukh, “Design and Preparation of Nematic Colloidal Particles,” *Langmuir* 38 (2022): 9099–9118.

34. H. Yoshida, Y. Tanaka, K. Kawamoto, et al., “Nanoparticle-Stabilized Cholesteric Blue Phases,” *Applied Physics Express* 2 (2009): 121501.

35. G. Cordoyiannis, V. S. Rao Jampani, S. Kralj, et al., “Different Modulated Structures of Topological Defects Stabilized by Adaptive Targeting Nanoparticles,” *Soft Matter* 9 (2013): 3956.

36. B. Senyuk, J. S. Evans, P. J. Ackerman, et al., “Shape-Dependent Oriented Trapping and Scaffolding of Plasmonic Nanoparticles by Topological Defects for Self-Assembly of Colloidal Dimers in Liquid Crystals,” *Nano Letters* 12 (2012): 955–963.

37. L. Tran, H.-N. Kim, N. Li, et al., “Shaping Nanoparticle Fingerprints at the Interface of Cholesteric Droplets,” *Science Advances* 4 (2018): eaat8597.

38. C. V. Rajaram, S. D. Hudson, and L. C. Chien, “Morphology of Polymer-Stabilized Liquid Crystals,” *Chemistry of Materials* 7 (1995): 2300–2308.

39. I. Dierking, L. L. Kosbar, A. Afzali-Ardakani, A. C. Lowe, and G. A. Held, “Two-Stage Switching Behavior of Polymer Stabilized Cholesteric Textures,” *Journal of Applied Physics* 81 (1997): 3007–3014.

40. A. Bosco, M. G. M. Jongejan, R. Eelkema, et al., “Photoinduced Reorganization of Motor-Doped Chiral Liquid Crystals: Bridging Molecular Isomerization and Texture Rotation,” *Journal of the American Chemical Society* 130 (2008): 14615–14624.

41. J. Baudry, M. Brazovskaia, L. Lejcek, P. Oswald, and S. Pirkl, “Arch-Texture in Cholesteric Liquid Crystals,” *Liquid Crystals* 21 (1996): 893–901.

42. R. Meister, H. Dumoulin, M.-A. Hallé, and P. Pieranski, “The Anchoring of a Cholesteric Liquid Crystal at the Free Surface,” *Journal De Physique II* 6 (1996): 827–844.

43. P. Rofouie, D. Pasini, and A. D. Rey, “Nano-Scale Surface Wrinkling in Chiral Liquid Crystals and Plant-Based Plywoods,” *Soft Matter* 11 (2015): 1127–1139.

44. D. M. Sussman and D. A. Beller, “Fast Scalable, and Interactive Software for Landau-de Gennes Numerical Modeling of Nematic Topological Defects,” *Frontiers in Physics* 7 (2019): 204.

45. J.-B. Fournier and P. Galatola, “Modeling Planar Degenerate Wetting and Anchoring in Nematic Liquid Crystals,” *Europhysics Letters* 72 (2005): 403–409.

46. N. Gribova, A. Arnold, T. Schilling, and C. Holm, “How Close to Two Dimensions Does a Lennard-Jones System Need to Be to Produce a Hexatic Phase?,” *Journal of Chemical Physics* 135, no. 5 (2011): 054514.

47. T. Kamal and S.-Y. Park, “A Liquid Crystal Polymer Based Single Layer Chemo-Responsive Actuator,” *Chemical Communications* 50 (2014): 2030–2033.

48. X. Wang, J. He, Q. Wei, et al., “Influence of Molecular Weight on Helical Twisting Power of Oligomer Chiral Dopants,” *Journal of Molecular Liquids* 339 (2021): 116816.

49. D. R. Nelson, *Defects and Geometry in Condensed Matter Physics* (Cambridge University Press, 2002).

Supporting Information

Additional supporting information can be found online in the Supporting Information section. **Supporting Fig. S1:** Transmission optical microscopy image between crossed polarizer and analyzer of a cholesteric droplet. The rubbing direction is parallel to the polarizer. The modulated texture appears between an anchoring parallel to the substrate and homeotropic at the interface with air. When the thickness changes, the color changes as well as the orientation of the stripes, which rotates by 180°. **Supporting Fig. S2:** Optical microscopy images of a PSCLC observed between crossed polarizers. In these images, we focus on one modulation period located between two dark stripes, delineated by black dashed lines. These lines are precisely positioned between two liquid crystal defects, identified as Defect 1 and Defect 2 in the first image (top left), which are visible in all other images. We rotated the sample between the crossed polarizers, varying the angle from 0° to 90°. Initially, the sample was aligned parallel to the polarizer (0°). The successive tilt angles relative to the polarizer are indicated at the top of each image. To facilitate the visualization of the stripe evolution as a function of polarization, the images were rotated to maintain a constant stripe orientation in all cases. **Supporting Fig. S3:** (a) Zoomed-in images of one modulation period of a PSCLC between crossed polarizers, showing the evolution of the stripes for different orientations (from 0° to 90°) relative to the polarizer. (b) Stripe segments extracted from the arch of a PSCLC with AuNPs in image (c). In both samples, it is observed that the dark stripe at 0° becomes thinner at 45° and then recovers its initial width at 90°, while the bright stripe at 0° splits into two with a thin dark stripe at 45° before returning to a single bright state at 90°. **Supporting Fig. S4:** Contrasted and superimposed PLM and SEM images showing an arch from a PSCLC-AuNPs sample. The associated table presents a quantitative analysis of the stripe tilt angles, correlated with the positions of the AuNPs according to different zones defined by their average relative orientation. The polarizer was aligned at 6° relative to the vertical, an orientation corresponding to the rubbing direction. **Supporting Fig. S5:** Correlation between a defect and AuNP accumulation. (Left) PLM image of a PSCLC-AuNP arch with a green line highlighting a defect where the stripe pattern becomes misaligned. (Right) Corresponding SEM image of the same region showing a high density of AuNPs strictly confined within this defect.